Figure 1. 1-T compact MRI system installed in the laboratory of an animal facility. The console (left) is placed in contiguity with the magnet (right).

system are small, and the fringe magnetic field is relatively weak. It can be installed in a small room that contains other electric or paramagnetic apparatuses. Cryogen refills are not needed, and the running cost is negligible. The openness of a permanent magnet system provides excellent accessibility to the sample in the magnet bore, which in turn makes it easy to position and monitor the sample. Because of these advantages, the system appears to be potentially applicable to routine small-animal experiments. In addition to high resolution, a short examination time is essential for routine experiments. The major problem is its relatively low magnetic field, which makes it difficult to achieve a sufficient signal-to-noise ratio (SNR) without excessive prolongation of the scan time because the magnetic field is a primary determinant of the SNR (10).

In this study we attempted to visualize living mice with the 1-T compact MRI system. We acquired images using a T1-weighted 3D fast low-angle shot (FLASH) sequence and investigated appropriate techniques to obtain images of acceptable quality in a reasonable imaging time. The principal aim of this study was to determine the applicability of the MRI system to routine experiments using mouse models.

MATERIALS AND METHODS
Instruments

Data were acquired on an MRmini system (MRTechnology, Tsukuba, Japan), consisting of a 1-T permanent magnet made of Nd-Fe-B material (Neomax, Osaka, Japan) and a compact console (Fig. 1). A solenoid coil of a 30-mm inner diameter was used. The specifications of the magnet were as follows: dimensions = 60 (W) × 64 (H) × 82 (D) cm, weight = 1400 kg, air gap = 10 cm, and magnetic field homogeneity = 3.6 ppm in a 30-mm diameter spherical volume. The maximum amplitude and slew rate of the gradient system were 70 mT/m and 350 T/m/second, respectively. The dimensions of the console were 52 (W) × 87 (H) × 60 (D) cm, and the total weight was about 100 kg. The horizontal 5-gauss line from the magnetic center was less than 1.2 m, and the

entire system, including the console, was installed in a space of 1.5×3 m^2, without magnetic shielding, in the laboratory of an SPF animal facility.

Animals

Female wild-type BALB/c mice, BALB/c nude mice, and severe combined immunodeficiency (SCID) mice were used for the animal experiments. All mice weighed about 25 g and were given food and water ad libitum. They were handled according to the guidelines of the host institution, and the experiments were approved by the committee for animal research at the institution.

Imaging Procedures

The mice were anesthetized with isoflurane inhalation and fixed on a polymethylmethacrylate holder in the prone position. The mouse and holder were tightly wrapped together with paper tape to reduce respiratory motion artifact. Coronal images of the entire trunk were obtained using a T1-weighted 3D FLASH sequence as localizer images. The scan parameters were as follows: repetition time (TR) = 30 msec, echo time (TE) = 3.6 msec, flip angle (FA) = 36°, in-plane matrix = 256 × 64, 32 slab partitions, number of excitations = 1, bandwidth = 50 kHz, and acquisition time = one minute two seconds. The in-plane pixel size was 0.26 mm × 0.52 mm, and slice thickness was 1.04 mm. If necessary the position of the mouse was changed, followed by additional acquisition of localizer images. After appropriate positioning was confirmed, images of higher spatial resolution were obtained in the coronal plane using a T1-weighted 3D FLASH sequence. The in-plane matrix was 256 × 128, and the in-plane pixel size was 0.26 × 0.26 mm. The slab thickness was fixed irrespectively of the number of slab partitions, and the slice thickness was 0.52 mm at 64 partitions. The TE was set at 3.6 and 6.7 msec for out-of-phase and in-phase imaging, respectively. The number of excitations was set at one for all data acquisitions to reduce scan time, and the bandwidth was 50 kHz. Other parameters are presented in the following sections. Because the Larmor frequency of

a high-field permanent magnet circuit using Nd-Fe-B material is sensitive to alterations in temperature, it was measured just before each acquisition to compensate for temperature-dependent drift.

Restraint of Respiratory Motion

The effect of respiratory motion on image quality was evaluated. Two wild-type mice and two nude mice were imaged with and without restraint of respiratory motion, which was achieved by tightly wrapping the mouse and holder together with paper tape. Two mice were imaged without wrapping first, and the remaining two were imaged with wrapping first. The scan parameters were as follows: TR = 40 msec, TE = 3.6 msec and 6.7 msec, FA = 57°, 64 partitions, and acquisition time = five minutes 28 seconds.

Slab Partition

To determine the appropriate number of slab partitions, two wild-type mice were imaged with eight, 16, 32, 64, and 128 partitions, resulting in acquisition times of 42 seconds, one minute 23 seconds, two minutes 45 seconds, five minutes 28 seconds, and 10 minutes 56 seconds, respectively, and slice thicknesses of 4.16, 2.08, 1.04, 0.52, and 0.26 mm, respectively. Other parameters were TR = 40 msec, TE = 3.6 msec, and FA = 57°. For phantom studies, a 50-mL tube containing copper sulfate solution, a sphere, and meshes was imaged with the same sets of imaging parameters.

TR and FA

The effect of TR and FA on image quality was examined. First we imaged a wild-type mouse successively, without changing the position of the mouse, using various values of TR and FA. The TRs used were 30, 40, and 50 msec, and the FAs used were 71°, 64°, 51°, 36°, and 28°. Data were acquired with TEs of 3.6 and 6.7 msec, and a total of 30 sets of images were obtained. The partition number was 32. The acquisition times were two minutes three seconds, two minutes 45 seconds, and three minutes 26 seconds for TRs of 30, 40, and 50 msec, respectively.

Next, 64-partition images were acquired for three wild-type mice and three nude mice using various TRs and FAs. The parameters used were TEs of 3.6 and 6.7 msec; TRs of 40, 50, and 60 msec; FAs of 64°, 57°, and 51°; and a total of 18 image sets were obtained successively for each mouse. The acquisition times were five minutes 28 seconds, six minutes 51 seconds, and eight minutes 13 seconds for TRs of 40, 50, and 60 msec, respectively.

Subcutaneous Tumor Xenografts

Visualization of subcutaneous tumor xenografts was evaluated. Two SCID mice were implanted in the left flank with 1×10^6 cells of human hepatocellular carcinoma cell line (HT17) mixed with matrigel (BD Biosciences, San Jose, CA, USA). After the tumors became palpable, MRI was performed. Two perpendicular diameters of the tumor (a: longer diameter; b: shorter diameter) were measured manually with a caliper, and tumor volume was calculated as $V = (\pi/6)ab^2$. The tumor volumes for the two mice were 77.2 and 207.2 mm^3 on the day of MRI. The parameters used for MRI were TE = 3.6 and 6.7 msec, TR = 40 msec, FA = 57°, 64 partitions, and acquisition time = five minutes 28 seconds. In addition, an SCID mouse was implanted in the left flank with 1×10^6 cells of human hepatocellular carcinoma cell line (Hep 3B) mixed with matrigel. The initial imaging study, using the parameters described above, was performed five weeks after implantation, followed by weekly imaging.

Data Analysis

For all experiments the image quality was evaluated visually by two radiologists. The SNR for the liver was calculated in some experiments. Regions of interest (ROIs) were manually drawn within the liver on three slices, avoiding the inclusion of signal voids corresponding to intrahepatic vessels, and the mean signal intensity (SI) of the liver was calculated. A rectangular ROI was also placed for the background region, and the standard deviation (SD) of the SI in the ROI was determined as noise. The SNR of the liver was defined as the ratio of the mean liver SI to noise. For all imaging sessions of the three mice bearing subcutaneous tumor xenografts, tumor volume was determined from MR images obtained with a TE of 6.7 msec. The contour of the tumor was traced manually on each slice in which the tumor was visualized, and tumor volume was calculated by summing the products of areas measured on each slice and slice thickness.

RESULTS

Restraint of Respiratory Motion

Restraining respiratory motion by tightly wrapping the mouse and holder together definitely improved the image quality, and highlighted the significance of respiratory motion in distorting the quality of 3D FLASH images (Fig. 2). In the absence of restraint, artificial stripes were evident in the craniocaudal direction, especially on images obtained with a TE of 6.7 msec.

Slab Partition

The images of mice obtained using eight partitions were of poor quality. Data acquisition using 32 or more partitions, corresponding to a slice thickness of ≤1.04 mm, provided images of acceptable quality. The liver SNR was calculated for the images of 32 or more partitions, with increases in the number of partitions depressing the mean SNR (27.0, 19.1, and 15.1 for 32, 64, and 128 partitions, respectively). The 128-partition images were relatively noisy on visual evaluation; however, they visualized the contour of organs clearly because of their high cross-sectional resolution, and were considered to be of acceptable quality for use in routine experiments (Fig. 3). Imaging of the tube phantom with eight partitions produced severe artificial inhomogeneity even in the center slice. The inhomogeneity in phantom imag-
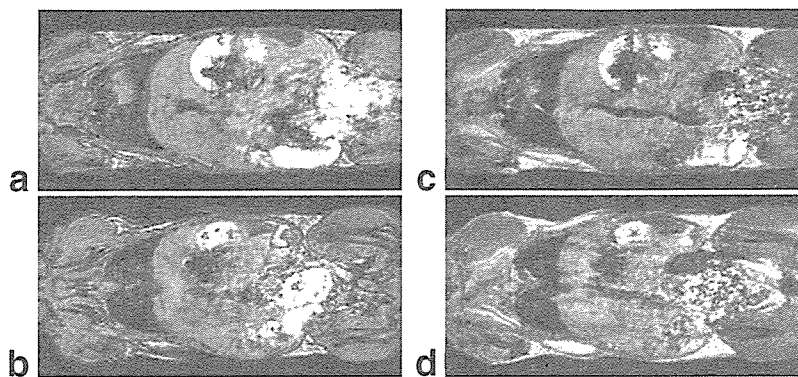
Figure 2. Coronal images of a mouse trunk obtained with (**a:** TE = 3.6 msec; **c:** TE = 6.7 msec) and without (**b:** TE = 3.6 msec; **d:** TE = 6.7 msec) restraint of respiratory motion. Artificial inhomogeneity in SI is reduced with restraint of respiratory motion. Signal void of the lung is displayed in the left part of each panel, and the pelvis is shown in the right part. The left side of the mouse is presented in the upper part of each panel.

ing was also reduced with increases in the number of partitions.

TR and FA

In imaging with 32 partitions and TE of 3.6 msec, a reduction in FA depressed the effect of noise visually but decreased image contrast (Fig. 4). Based on the balance between noise reduction and preservation of contrast, FA = 51–64° was judged to be appropriate. Longer TR also reduced the effect of noise at the expense of prolongation of acquisition time. Similar effects of TR and FA were shown for imaging with TE = 6.7 msec.

The SNRs for the liver on 64-partition images increased with increasing TR or decreasing FA (Fig. 5). Whereas a dependence of noise and contrast on TR and FA similar to that in 32-partition imaging was noted,

each combination of TR and FA offered 64-partition images of acceptable quality in all mice. The liver, spleen, kidneys, lungs, heart, gallbladder, adrenal glands, ovaries, inguinal lymph nodes, and limb muscles were visualized (Fig. 6). Artificial inhomogeneity in the liver was often shown on images obtained with TE = 6.7 msec, and the liver was better delineated on images obtained with TE = 3.6 msec. The visualization of the kidneys was sometimes affected by artifacts that presumably were related to peristalsis, which was reduced with decreasing FA.

Subcutaneous Tumor Xenografts

In all three mice bearing subcutaneous tumor xenografts, the tumors were clearly delineated on images obtained with TE = 3.6 msec and 6.7 msec. They were well demarcated by hyperintense subcutaneous fat on
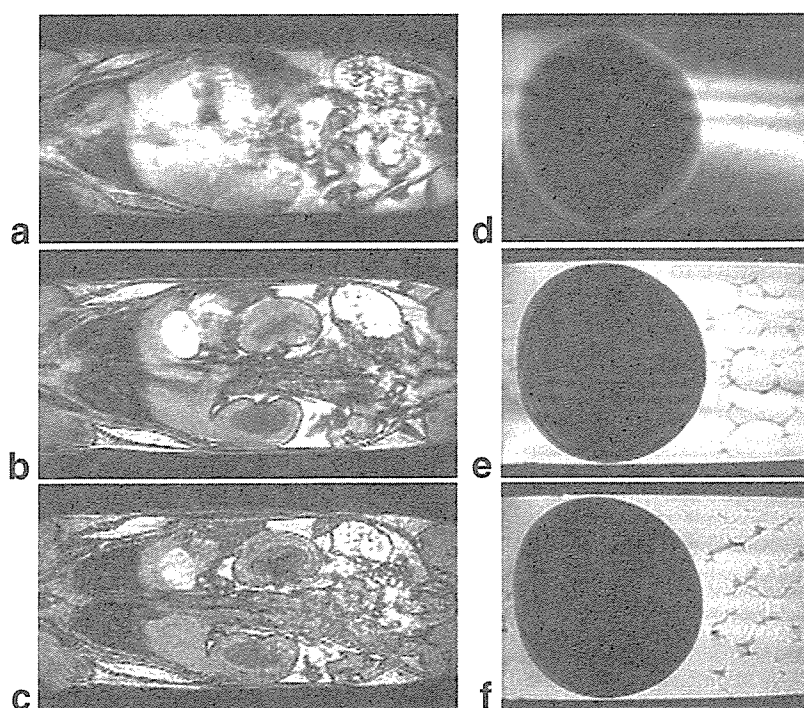
Figure 3. Mouse images obtained with eight (**a**), 32 (**b**), and 128 (**c**) partitions, and phantom images with eight (**d**), 32 (**e**), and 128 (**f**) partitions. Severe artificial inhomogeneities in SI are shown for the eight-partition images of both the mice and the phantom.
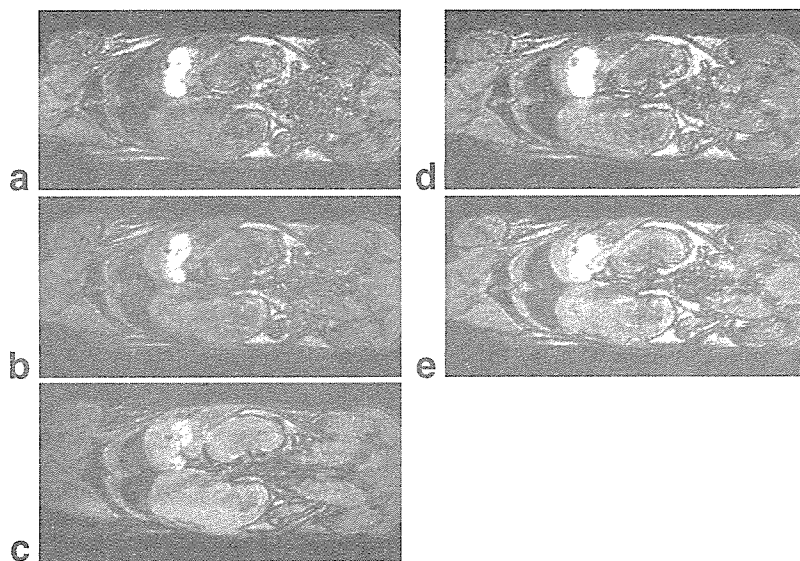
Figure 4. Effect of TR and FA in mouse imaging. Images were obtained with TR/FA = 40/71° (a), 40/51° (b), 40/28° (c), 30/51° (d), and 50/51° (e). A decrease in FA and increase in TR made the images less noisy; however, imaging with TR/FA = 40/28° yielded poor-contrast images.

images obtained with TE = 6.7 msec, resulting in easier recognition of the contours than on images obtained with TE = 3.6 msec. The tumor volumes obtained by the MR measurement (88.4 and 197.0 mm³) were similar to those obtained by the caliper measurement (77.2 and 207.2 mm³, respectively). In the mouse that was assessed serially, tumor growth was observed on the MR images visually and quantitatively (Fig. 7).

DISCUSSION

We examined the feasibility of imaging living mice on a 1-T compact MRI system and investigated appropriate imaging techniques. Although the system offers substantial convenience, the relatively low magnetic field impairs its ability to attain a high SNR (10). To overcome this problem, a small solenoid coil with many turns is used in the system because the SNR attained with a solenoid coil is approximately three times better than that attained with a saddle-shaped coil (10). The imaging sequence used was a 3D FLASH sequence, which can provide high-resolution, contiguous slices in a reasonable time (11,12). Motion artifacts may cause degradation of the 3D FLASH images in living subjects (11). We demonstrated that restraint of respiratory motion, achieved by a simple technique, definitely improves image quality. A FLASH sequence is sensitive to

magnetic field inhomogeneities (13). Severe artifacts occurred when the phantom and mice were imaged with a small number of slab partitions, which apparently were attributable to intraslice inhomogeneity in the magnetic field enhanced by thickening of a slice. An increase in the partition number and consequent decrease in slice thickness reduced the artifact, and the image quality was acceptable when a slice thickness of ≤1.04 mm (32 or more partitions) was used. To achieve a sufficient SNR, preserved image contrast, and short acquisition time simultaneously, the effect of TR and FA on image quality was assessed, and appropriate values were defined. Using the determined parameters and techniques, we were able to obtain thin-slice 3D images covering the entire trunk of a mouse within a practical acquisition time and visualize various organs, including the liver, spleen, lung, and kidneys, consistently.

In this study the typical voxel size was 0.26 × 0.26 × 0.52 mm. Although images with higher in-plane resolution were acquired in some previous studies (14,15), in other studies the in-plane resolution was comparable to ours (6,16,17). Because we used a 3D sequence, the slice thickness, which is another important determinant of spatial resolution, was relatively thin. The spatial resolution required is dependent on the target of a particular study, and the spatial resolution in our study appears to be acceptable for various experimental
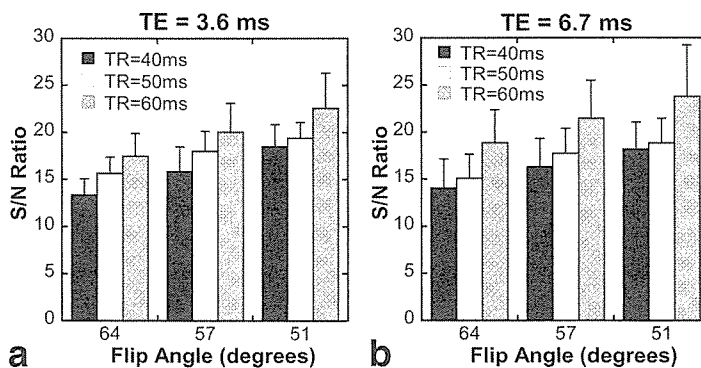
Figure 5. The SNR for the liver with TE = 3.6 (a) and 6.7 msec (b). The SNR increased with increasing TR and decreasing FA.
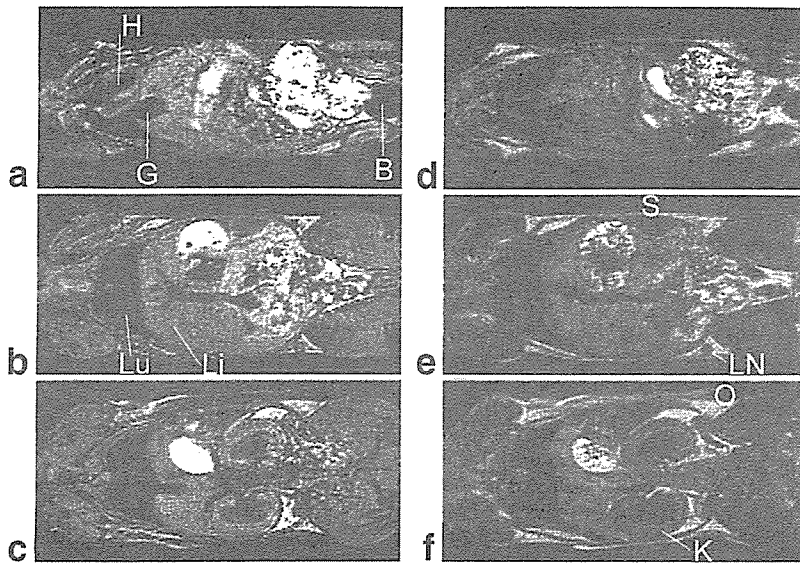
Figure 6. Images of a mouse obtained with TR/TE/FA = 40/3.6/57° (a–c) and 40/6.7/64° (d–f). H = heart, G = gallbladder, B = urinary bladder, Lu = lung, Li = liver, S = spleen, LN = inguinal lymph node, O = ovary, K = kidney.

applications. Spatial resolution can be improved at the expense of prolongation of scan time. However, routine laboratory experiments often require the use of many mice, and it is essential to acquire images of one mouse in a short time period. The imaging time required to cover the entire trunk with a spatial resolution of 0.26 × 0.26 × 0.52 mm was typically five minutes 28 seconds, and the total experiment time, from the start of induction of anesthesia to the end of data acquisition, was less than 20 minutes. The openness of a permanent magnet system, and placement of the magnet near other electric or paramagnetic apparatuses offer significant convenience for preparation, positioning, and monitoring of mice and operation of the instruments, which contributes to shortening the total experiment time and facilitating routine use of MRI.

Subcutaneous tumor xenografts were clearly visualized in this study. The volume of a subcutaneous tumor is commonly estimated by measuring two or three diameters manually with a caliper. The tumor volumes estimated from MRI were comparable to those obtained by the caliper measurement, and tumor growth could be followed on the MR images. The calculation of volume by the caliper measurement is based on the assumption of a simple shape and may be erroneous due to atypical morphology of a tumor (18). MRI delineates

the entire tumor on thin-slice, contiguous images and does not require any geometric assumption for volume calculation. It appears to provide a reliable estimate of tumor volume irrespectively of the shape. While MRI is especially useful for visualizing internal organs and tumors located in deep sites, it may also aid in evaluating the morphology of subcutaneous tumors.

Versatility is one of the major advantages of MRI. Because the MR signal is influenced by a number of parameters, including proton density, T1 relaxation time, T2 relaxation time, magnetic susceptibility, water diffusion, and blood flow, images containing various kinds of anatomical and functional information can be acquired depending on the imaging sequences and parameters used. In this study we demonstrated the feasibility of T1-weighted FLASH imaging with the compact system, and its ability to visualize various organs and subcutaneous tumors. The applicability and utility of other imaging techniques using this system remain to be investigated. Experiments on microcirculation and cardiovascular function often require a combination of high temporal resolution and high spatial resolution, and it would be difficult to satisfy the requirements using the low-field system. The administration of contrast media also extends the usefulness of MRI. Intrinsic image contrast using a FLASH sequence is
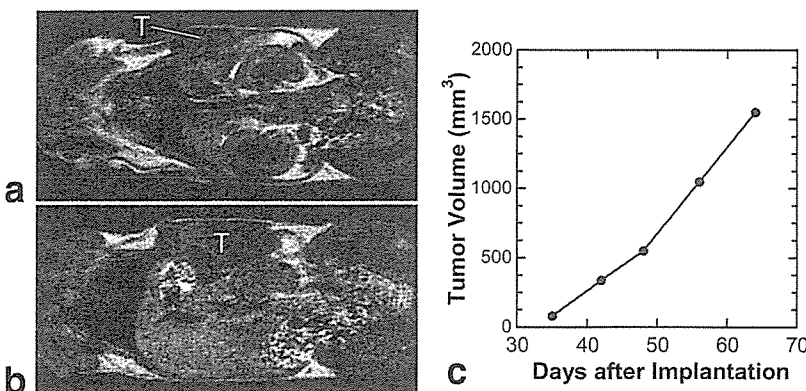
Figure 7. Images of a mouse bearing subcutaneous tumor xenograft (T) acquired five (a) and seven (b) weeks after implantation. The tumor volumes measured on MR images were plotted against the number of days after implantation (c).

lower than that obtained with a spin-echo sequence, and the use of contrast media is especially helpful in FLASH imaging (19). The contrast effect depends on the magnetic field strength (20), and the similarity in magnetic field between the compact MRI system and common clinical scanners may facilitate an exchange of information between clinical practice and experiments on the system.

In conclusion, we have demonstrated the feasibility of imaging living mice with a 1-T compact MRI system, and determined the appropriate imaging techniques. The system provides images of living mice with acceptable quality and within a reasonable time, and is expected to be useful for routine experiments on mouse models.

REFERENCES

1. Marzola P, Sbarbati A. Magnetic resonance imaging in animal models of pathologies. Methods Enzymol 2004;386:177–200.
2. Pautler RG. Mouse MRI: concepts and applications in physiology. Physiology (Bethesda) 2004;19:168–175.
3. Beckmann N, Mueggler T, Allegrini PR, Laurent D, Rudin M. From anatomy to the target: contributions of magnetic resonance imaging to preclinical pharmaceutical research. Anat Rec 2001;265:85–100.
4. Chatham JC, Blackband SJ. Nuclear magnetic resonance spectroscopy and imaging in animal research. ILAR J 2001;42:189–208.
5. Klaunberg BA, Lizak MJ. Considerations for setting up a small-animal imaging facility. Lab Anim (NY) 2004;33:28–34.
6. Kobayashi H, Kawamoto S, Brechbiel MW, et al. Micro-MRI methods to detect renal cysts in mice. Kidney Int 2004;65:1511–1516.
7. Smirnov P, Gazeau F, Lewin M, et al. In vivo cellular imaging of magnetically labeled hybridomas in the spleen with a 1.5-T clinical MRI system. Magn Reson Med 2004;52:73–79.
8. Gupta S, Adhami VM, Subbarayan M, et al. Suppression of prostate carcinogenesis by dietary supplementation of celecoxib in trans-
   genic adenocarcinoma of the mouse prostate model. Cancer Res 2004 1;64:3334–3343.
9. Haishi T, Uematsu T, Matsuda Y, Kose K. Development of a 1.0 T MR microscope using a Nd-Fe-B permanent magnet. Magn Reson Imaging 2001;19:875–880.
10. Hoult DI, Richards RE. The signal-to-noise ratio of the nuclear magnetic resonance experiment. J Magn Reson 1976;24:71–85.
11. Ross JS, Masaryk TJ, Modic MT. Three-dimensional FLASH imaging: applications with gadolinium-DTPA. J Comput Assist Tomogr 1989;13:547–552.
12. Frahm J, Haase A, Matthaei D. Rapid three-dimensional MR imaging using the FLASH technique. J Comput Assist Tomogr 1986;10:363–368.
13. Winkler ML, Ortendahl DA, Mills TC, et al. Characteristics of partial flip angle and gradient reversal MR imaging. Radiology 1988;166:17–26.
14. Hensley HH, Chang WC, Clapper ML. Detection and volume determination of colonic tumors in Min mice by magnetic resonance micro-imaging. Magn Reson Med 2004;52:524–529.
15. Kobayashi H, Jo SK, Kawamoto S, et al. Polyamine dendrimer-based MRI contrast agents for functional kidney imaging to diagnose acute renal failure. J Magn Reson Imaging 2004;20:512–518.
16. Denis MC, Mahmood U, Benoist C, Mathis D, Weissleder R. Imaging inflammation of the pancreatic islets in type 1 diabetes. Proc Natl Acad Sci USA 2004 24;101:12634–12639.
17. Brooks KJ, Hill MD, Hockings PD, Reid DG.. MRI detects early hindlimb muscle atrophy in Gly93Ala superoxide dismutase-1 (G93A SOD1) transgenic mice, an animal model of familial amyotrophic lateral sclerosis. NMR Biomed 2004;17:28–32.
18. Kiessling F, Heilmann M, Vosseler S, et al. Dynamic T1-weighted monitoring of vascularization in human carcinoma heterotransplants by magnetic resonance imaging. Int J Cancer 2003;104:113–120.
19. Runge VM, Wood ML, Kaufman D, Price AC. Gd DTPA. Future applications with advanced imaging techniques. Radiographics 1988;8:161–179.
20. Rinck PA, Muller RN. Field strength and dose dependence of contrast enhancement by gadolinium-based MR contrast agents. Eur Radiol 1999;9:998–1004.

Characterization of monoclonal antibodies directed against the canine distemper virus nucleocapsid protein

Munemitsu Masuda [a], Hiroki Sato [b], Hiroshi Kamata [c],
Tomoe Katsuo [b], Akiko Takenaka [b], Ryuichi Miura [b],
Misako Yoneda [b], Kyoko Tsukiyama-Kohara [b],
Kiyohisa Mizumoto [a], Chieko Kai [b,*]

[a] Department of Biochemistry, School of Pharmaceutical Sciences, Kitasato University,
Shirokane, Minato-ku, Tokyo 108-8641, Japan
[b] Laboratory of Animal Research Center, Institute of Medical Science, University of Tokyo,
4-6-1 Shirokanedai, Minatoku, Tokyo 108-8639, Japan
[c] Department of Veterinary Medicine, College of Bioresource Sciences, Nihon University,
Kameino 1866, Fujisawa, Kanagawa 252-8510, Japan

Abstract

We have established four monoclonal antibodies (MAbs) against the nucleocapsid protein (NP) of canine distemper virus (CDV). A competitive binding assay has revealed that the MAbs are directed against two antigenic domains. An immunofluorescence assay using a series of deletion clones of the NP and an immunoprecipitation assay using the NP have revealed that two of the MAbs recognize the C-terminal region of the NP while the other two recognize the tertiary structure of the N-terminal domain. These MAbs reacted with all eight strains of CDV used in this study, but showed different reactivities against measles virus and rinderpest virus.
© 2006 Elsevier Ltd. All rights reserved.

Keywords: Canine distemper virus; Nucleocapsid protein; Monoclonal antibodies; Deletion mutants; Antigenic domain; Competitive ELISA

* Corresponding author. Tel.: +81 3 5449 5497; fax: +81 3 5449 5397.
E-mail address: ckai@ims.u-tokyo.ac.jp (C. Kai).

1. Introduction

Canine distemper virus (CDV) is a member of the genus *Morbillivirus* of the family *Paramixoviridae*. In all negative stranded RNA viruses, including the Paramyxoviruses, the genomic RNA is tightly bound to the nucleocapsid protein (NP), the major structural protein, in the form of a helical nucleocapsid [1]. This structure is a template required for both replication and transcription and comprises the ribonucleoprotein complex in conjunction with the viral large protein (L) and phosphoprotein (P) [2]. NPs are the most abundant viral proteins and highly conserved in the genus *Morbillivirus* [1]. Recently, the number of dogs showing typical clinical signs of CDV infection has been increasing, despite the fact that most of these dogs had been vaccinated [3]. Genetic variations in the *NP* gene have notably found in the field isolates [4]. It is therefore important for the characterization of recent field isolates of CDV to investigate the antigenic domains and genetic variations in the *CDV-NP* gene. However, only a few reports about preparation and characterization of monoclonal antibodies against CDV-NP have been reported previously [5,6], and only limited numbers of them are currently available for antigenic studies of CDV. In this study, we newly established four monoclonal antibodies (MAbs) against the NP of CDV-Onderstepoort strain and determined the antigenic regions of these antibodies by competitive binding assay and immunofluorescence assay (IFA). In addition, we compared these MAbs with the two MAbs against the NP of CDV-FXNO strain, which were previously established by Hirayama et al. [6]. Furthermore, we examined the reactivity of the four MAbs with other strains of CDV as well as those of other morbilliviruses, namely, measles virus (MV) and rinderpest virus (RPV).

2. Material and methods

2.1. Cells and virus

Vero cells were cultured in Dulbecco's modified Eagle's medium (DMEM) supplemented with 100 U/ml of penicillin G, 100 μg of streptomycin (GIBCO BRL, USA), and 5% fetal bovine serum (FBS; SIGMA, USA). COS-7 cells were cultured in a culture medium whose composition was the same as above except that it contained 10% FBS. B95a cells were cultured in RPMI-1640 medium supplemented with 100 U/ml of penicillin G, 100 μg of streptomycin, and 5% FBS. Five strains (Onderstepoort, FXNO, YSA, Snyder–Hill, and haku93) of CDV, the Edmonston strain of MV, the RBOK strains of RPV were propagated in Vero cells. Three strains (Yanaka, tanu, haku00) of CDV, the HL strain of MV, the L strain of RPV were propagated in B95a cells.

2.2. Hybridoma production and MAb screening

CDV-infected Vero cells showing 80–90% cytopathic effects (c.p.e.) were harvested, frozen and thawed, sonicated at 20 kHz for 30 s and clarified by centrifugation at 6000 rpm to prepare immunizing materials. MAbs were produced as described previously [7] with some modifications. Briefly, spleen cells obtained from CDV-immunized

BALB/c mice were fused with myeloma cells using polyethylene glycol 4000. The hybridoma cells were screened for antibody production against CDV using an indirect immunoperoxidase (IIP) test. Positive cells were cloned by the limiting dilution method and were inoculated intraperitoneally into pristane-primed BALB/c mice. For comparing with the four MAbs isolated in this study, MAbs c-5 and h-6 against the NP of CDV-FXNO strain [6] were used.

2.3. Radioimmunoprecipitation assay

The specificity of the MAbs was determined by radioimmunoprecipitation assay (RIPA) as described previously [8]. Briefly, virus-infected cells or mock-infected cells were radiolabeled with 3 MBq/ml[^{35}S]methionine and cystein (Amersham Bioscience) for 2 h. The cells were lysed with lysis buffer (0.5% TritonX-100, 0.5% sodium deoxycholate, and 5 mM NaCl). An aliquot of cell lysate was subjected to thermal denaturation by boiling for 5 min and was then reacted with the anti-NP MAbs for 3 h at 4 °C, followed by incubation with protein A beads. The immunoprecipitates were resolved by 10% SDS-polyacrylamide gel electrophoresis (SDS-PAGE).

2.4. Competitive binding assay

Antibodies (IgG) were precipitated in the ascitic fluid from hybridoma-inoculated mice containing 33% ammoniumsulphate precipitation and were then dialyzed against phosphate buffered saline (PBS). The IgG was biotinylated using a biotin labeling kit (Roche) according to the manufacture's instructions. Vero cells which had been infected with the Onderstepoort strain of CDV and showed 70–80% c.p.e. in 100-mm diameter culture dishes were lysed with 0.5 ml of lysis buffer (0.5% TritonX-100, 0.5% sodium deoxycholate, and 5 mM NaCl) and centrifuged at 5000 rpm for 3 min. Ninety-six-well microplates were coated with the supernatant for 1 h at room temperature as viral antigens for ELISA. An aliquot of the unlabeled MAbs was serially diluted fourfold, and aliquots of each dilution were placed in wells of the plates. After 1 h incubation at room temperature, the plates were washed three times with 0.05% Tween 20-PBS. A 0.05 ml aliquot of biotinylated MAb was diluted to an approximate OD of 0.1 added to each well and allowed to bind for 1 h at room temperature. The plates were washed three times again, followed by · incubation with HRP-conjugated streptavidin (Roche) at a 1:1000 dilution for 1 h at room temperature. Then again the plates were washed three times and visualized with a TMB peroxidase EIA substrate kit (BIO-RAD) according to the manufacture's instructions. After 30 min, OD was measured at 655 nm with a microplate reader (BIO-RAD).

2.5. Construction and eukaryotic expression of NP and deletion mutants

Vero cells were inoculated with the Onderstepoort strain of CDV and were incubated for 18 h. Total RNA was then extracted using ISOGEN (Nippon Gene) according to the manufacture's instructions. One microgram of total RNA was reverse transcribed with SuperScript II reverse transcriptase (GIBCO BRL) in the presence of the antisence primer, P2 (1570–1587 nt position of *NP* gene). The resulting cDNA was amplified by PCR with

F1 sense primer (1–21 nt position of *NP* gene) and P2 antisence primer using LA-Taq DNA polymerase (TaKaRa). The amplified product was subcloned into pBluescript SK-vector, digested with *Xba* I and *Xho* I, and then inserted into pME-18S mammalian expression vector, designated as pME-ON. To create deletion clones of the NP, pME-ON was PCR amplified with a set of primers (described below) using *pfu turbo* DNA polymerase (Stratagene) according to the manufacture's instructions (NP-D1 sense 5′-gtggaatcccctggacaatt-3′, NP-D1 antisense 5′-catattggtaggtctgaacc-3′; NP-D2 sense 5′-atgaggagatggattaagtat-3′, NP-D2 antisense 5′-gaacaaggagaggatactgat-3′; NP-D3 sense 5′-atgatttgtgatatagataac-3′, NP-D3 antisense 5′-ctccgagtcggctgcagtatc-3′; NP-D4 sense 5′-atgggagttggtgttgaacttgaaaactca-3′, NP-D4 antisense 5′-ttcagcaattctaggcttgtt-3′; NP-D5 sense 5′-taaatattcaagaccagtcttgcatcagt-3′, NP-D5 antisense 5′-agcataactccagag-tagtgg-3′). PCR products were phosphorylated using a DNA kination kit (TOYOBO) and were self-ligated using a DNA ligation kit (TaKaRa). Nucleotide sequences of these constructs were confirmed by DNA sequencing (ABI PRISM 377 DNA sequencer).

COS-7 cells were seeded into 35-mm diameter culture dishes and grown until semi-confluent, and 1 μg of plasmid DNAs were transfected using FuGENE6 (Roche) according to the manufacture's instructions. After 24 h, cells were fixed with acetone and analyzed by indirect immunofluorescence assay (IFA) as described below.

2.6. IFA

Vero cells and B95a cells were infected with various strains of *Morbilliviruses* described above. When approximately 50% c.p.e. was observed, the cells were fixed with acetone for 30 min at room temperature, followed by incubation in a 1:1000 dilution of the ascitic fluids for 1 h at 37 °C. After washing in PBS, cells were incubated in a 1:500 dilution of fluorescein isothiocyanate (FITC)-conjugated anti-mouse IgG (ICN Biomedicals, Inc.) for 1 h at 37 °C. After washing in PBS, fluorescence was observed with a fluorescent microscope (Olympus).

3. Results

3.1. Specificity of the MAbs for CDV-NP

To obtain MAbs against the CDV-NP, mice were immunized with the Onderstepoort strain of CDV, and the hybridoma cells were established and screened, as described in Section 2. The specificity of the MAbs so obtained was determined by RIPA (Fig. 1). Four of the MAbs (2B, 7G, 8G, 3) detected a 58 kDa protein in the CDV-infected Vero cells. These results indicate that these four MAbs recognize the CDV-NP.

3.2. Analysis of the antigenic domains by competitive binding assay

To determine the antigenic domain(s) recognized by the four MAbs, we performed a competitive binding assay using the biotinylated MAbs. As shown in Table 1, two antigenic domains were identified: domain I was recognized by MAbs 2B and 3, and
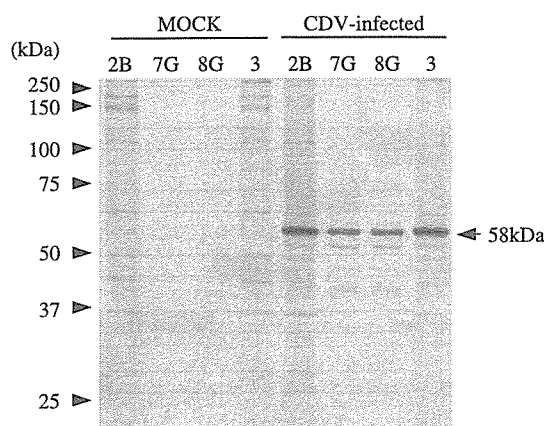
Fig. 1. Radioimmunoprecipitation assay (RIPA) of [^{35}S]methionine-labeled CDV viral proteins using MAbs. MOCK and CDV-infected Vero cells were metabolically labeled with ^{35}S-Met/Cys, then subjected to RIPA with MAb 2B, 7G, 8G, 3. The NP is indicated by arrow head (58 kDa).

domain II by MAbs 7G and 8G. Two other MAbs (c-5 and h-6), which were previously established by Hirayama et al. [6] and are directed against the NP of CDV-FXNO strain, were also tested by the same competitive binding assay. MAb h-6 recognized domain II in the same manner as MAbs 7G and 8G. On the other hand, MAb c-5 showed no competition with any other MAbs. MAb c-5 thus seems to recognize a distinct antigenic domain.

3.3. Mapping of the epitope regions in NP

To determine the epitope regions in the NP recognized by these MAbs, we constructed a series of deletion clones of the NP gene of the CDV Onderstepoort

Table 1
Analysis of the antigenic domains by competitive binding assay

Purified MAb	Antigenic domain	Biotinylated MAb					
		2B	3	7G	8G	h-6	c-5
2B	I	+[a]	+	−	−	−	−
3	I	+	+	−	−	−	−
7G	II	−	−	+	+	+	−
8G	II	−	−	+	+	+	−
h-6[b]	II	−	−	+	+	+	−
c-5[b]	III	−	−	−	−	−	+

A constant dilution of the biotinylated MAbs was incubated with a 1:4, 1:16, 1:64, 1:256 and 1:1024 dilution of each non-labeled MAb. Using the streptavidin HRP-conjugated, competition was determined as a reduction of the fixation of the conjugate by more than 80%.
[a] +, IFA positive; −, IFA negative.
[b] Previously reported MAb.

(a.a.)

```
                                                    1                              523
                        Full length   [                                              ]

                                       1   8
                        NP-D1          [▓▓▓                                           ]

                                          81      192
                        NP-D2          [   ▓▓▓▓▓                                       ]

                                              193    252
                        NP-D3          [         ▓▓▓▓                                  ]

                                                  253    336
                        NP-D4          [            ▓▓▓▓▓                              ]

                                                          359          523
                        NP-D5          [                    ▓▓▓▓▓▓▓▓▓▓▓▓ ]
```
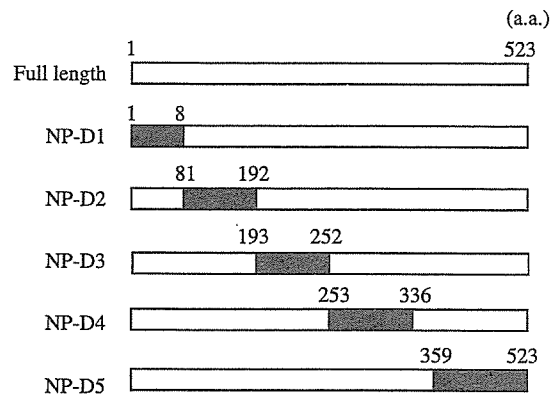
Fig. 2. *NP* gene and the series of its deletion clones of CDV strain Onderatepoort. These clones were inserted to eucaryotic expression vector pME-18S. The deleted regions of *NP* gene are indicated as filled bar. The number indicates amino acid residues.

strain as summarized in Fig. 2. These clones were expressed in COS-7 cells, and an IFA was performed using the four MAbs. MAbs 2B and 3 reacted with NP deletion clones D1 through D4 but not with D5 (Table 2). This suggests that MAbs 2B and 3 recognized the C-terminal region of the NP (a.a.359–523). Interestingly, this non-reactivity with NP-D5 is also shared by MAb c-5, which exhibited no competition with any other MAbs in the competitive binding assay. MAbs 7G, 8G and h-6 reacted only with NP-D5, indicating that they recognize an epitope on the protein expressed from the *NP* gene (a.a.1–336). However, none of NP clones D1 through D4 were recognized by these three MAbs. It is thus possible that these MAbs recognize the tertiary structure of the NP. To clarify this possibility, ^{35}S-labeled cell lysate infected with CDV was thermally denatured by boiling and was then subjected to RIPA. As shown in Fig. 3, the reactivity with the denatured NP was greatly reduced in MAbs 7G and 8G. These results indicate that MAbs 7G and 8G recognize the epitope in the NP's N-terminal domain which has a tertiary structure.

Table 2
Mapping of the epitope regions on NP

MAb	Control	Full length	D1	D2	D3	D4	D5
2B	−[a]	+	+	+	+	+	−
3	−	+	+	+	+	+	−
7G	−	+	−	−	−	−	+
s8G	−	+	−	−	−	−	+
h-6[b]	−	+	−	−	−	−	+
c-5[b]	−	+	+	+	+	+	−

[a] +, IFA positive; −, IFA negative.
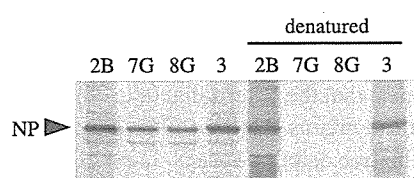[b] Previously reported MAb.

Fig. 3. RIPA with denatured or undenatured condition, using the four MAbs 2B, 7G, 8G 3. The immune complexes were electrophoresed in 10% SDS-PAGE and auto-radiographed by means of FUJIFILM BAS-1500. The NP is indicated by arrow head (58 kDa).

3.4. Immunoreactivity of anti-CDV NP MAbs with various strains of Morbillivirus

All four MAbs were examined for their cross-reactivity with various strains of *Morbilliviruses* using an IFA test. As summarized in Table 3, all MAbs reacted with all tested strains of CDV. In contrast, only MAbs 7G and 8G showed cross-reactivities with two strains (the Edmonston, HL) of MV and the RBOK strain of RPV, while MAbs 2B and 3 failed to show any cross-reactivity. None of the MAbs showed reactivity with the L strain of RPV.

4. Discussion

We obtained four MAbs directed against the NP of the CDV Onderstepoort strain. In the competitive binding assay, these four MAbs recognized a total of two antigenic domains. In addition, MAb c-5 against the NP of the CDV FXNO strain displayed no competition with any other MAbs. These results indicate that at least three distinct antigenic domains exist in the CDV-NP. The reactivities with the NP deletion clones revealed that MAbs 2B and 3

Table 3
Immunoreactivity of anti-CDV NP MAbs with various strains of *Morbillivirus*

Virus	Isolate/strain	Control	2B	3	7G	8G
CDV	Onderste-poort	−[a]	+	+	+	+
	YSA	−	+	+	+	+
	Snyder–Hill	−	+	+	+	+
	FXNO	−	+	+	+	+
	Yanaka	−	+	+	+	+
	Tanu	−	+	+	+	+
	Haku93	−	+	+	+	+
	Haku00	−	+	+	+	+
MV	Edmonston	−	−	−	+	+
	HL	−	−	−	+	+
RPV	RBOK	−	−	−	+	+
	L	−	−	−	−	−

[a] +, IFA positive; −, IFA negative.

recognize the C-terminal region of the NP (a.a.359–523). Interestingly, this reactivity with the C-terminal region of the NP is shared by MAb c-5, which recognized a unique antigenic domain. These results suggest that the C-terminal (a.a. 359–523) of the CDV-NP harbors at least two distinct antigenic domains. On the other hand, MAbs 7G and 8G showed no reactivity against four of the five deletion clones. In addition, after thermal denaturation of the NP, the reactivity with the NP disappeared in MAbs 7G and 8G. These results strongly suggest that antigenic domain I consists of the tertiary structure of the N-terminal region. Previous reports describe that the 400 N-terminal residues form a globular structure and that the C-terminal region appears to be a tail extending from the surface of the globular body [9–11]. It seems reasonable to explain that MAbs 7G and 8G recognize an epitope located on the surface of the globular structure of the NP.

All strains of CDV used in this study reacted with all four MAbs (2B, 7G, 8G and 3) (Table 3). In contrast, the Edmonston and HL strains of MV and the RBOK strain of RPV reacted with MAbs 7G and 8G but not with MAbs 2B and 3. The N-terminal 80% of the NP is highly conserved among the morbilliviruses [1]. The 400 N-terminal residues of the NP of the CDV Onderstepoort strain displayed 81.4, 81.2 and 81.5% homology to those of the MV Edmonston and HL strains and the RPV RBOK strain, respectively. On the other hand, the remaining C-terminal region of the NP is poorly conserved among the morbilliviruses [12]; the C-terminal region (a.a.400–523) of the NP of the CDV Onderstepoort strain has only 25.4, 25.6 and 26.4% homology to the equivalent NP regions of MV Edmonston and HL strains and the RPV RBOK strain, respectively. This variability in the C-terminal region may cause antigenic heterogeneity among morbilliviruses, which is in agreement with the results of this study. On the other hand, the L strain of RPV showed no reactivity with any of the four MAbs. This lapinized strain of RPV was derived from a wild-type strain after numerous passages through rabbits [13]. The homology between the NP of the CDV Onderstepoort strain and that of the RPV L strain is 68.0%. The antigenicity of the NP of RPV may be different from those of other morbilliviruses.

A previous report demonstrated that in the family *Paramixoviridae* the C-terminal region of the NP interacts with the viral L and P proteins and controls viral genome replication and transcription [2]. On the other hand, the N-terminal globular domain of the NP interacts with viral genome after completion of the folding process [14]. Previously, Gombert et al. reported the kinetics of conformational maturation of MV-NP using a monoclonal antibody, which recognizes a conformational epitope on NP, and antiserum, which recognizes a less folded form of NP [14]. However, there is no report for MAbs, which recognize a conformational epitope on CDV-NP. In this study, we obtained MAbs that recognize the tertiary structure of the N-terminal region and linear epitopes in the C-terminal region of the CDV-NP. These MAbs are expected to be powerful tools for further detailed functional analysis of the CDV-NP.

Acknowledgements

References

[1] Parks GD, Ward CD, Lamb RA. Molecular cloning of the NP and L genes of simian virus 5: identification of highly conserved domains in paramyxovirus NP and L proteins. Virus Res 1992;22(3):259–79.

[2] Horikami SM, Curran J, Kolakofsky D, Moyer SA. Complexes of Sendai virus NP-P and P-L proteins are required for defective interfering particle genome replication in vitro. J Virol 1992;66(8):4901–8.

[3] Gemma T, Watari T, Akiyama K, Miyashita N, Shin YS, Iwatsuki K, et al. Epidemiological observations on recent outbreaks of canine distemper in Tokyo area. J Vet Med Sci 1996;58(6):547–50.

[4] Shin Y, Mori T, Okita M, Gemma T, Kai C, Mikami T. Detection of canine distemper virus nucleocapsid protein gene in canine peripheral blood mononuclear cells by RT-PCR. J Vet Med Sci 1995;57(3):439–45.

[5] Orvell C, Sheshberadaran H, Norrby E. Preparation and characterization of monoclonal antibodies directed against four structural components of canine distemper virus. J Gen Virol 1985;66(Pt 3):443–56.

[6] Hirayama N, Senda M, Nakashima N, Takagi M, Sugiyama M, Yoshikawa Y, et al. Protective effects of monoclonal antibodies against lethal canine distemper virus infection in mice. J Gen Virol 1991;72(Pt 11): 2827–30.

[7] Sugiyama M, Minamoto N, Kinjo T, Hirayama N, Sasaki H, Yoshikawa Y, et al. Characterization of monoclonal antibodies against four structural proteins of rinderpest virus. J Gen Virol 1989;70(Pt 10): 2605–13.

[8] Yoshida E, Shin YS, Iwatsuki K, Gemma T, Miyashita N, Tomonaga K, et al. Epitopes and nuclear localization analyses of canine distemper virus nucleocapsid protein by expression of its deletion mutants. Vet Microbiol 1999;66(4):313–20.

[9] Compans RW, Mountcastle WE, Choppin PW. The sense of the helix of paramyxovirus nucleocapsids. J Mol Biol 1972;65(1):167–9.

[10] Heggeness MH, Scheid A, Choppin PW. The relationship of conformational changes in the Sendai virus nucleocapsid to proteolytic cleavage of the NP polypeptide. Virology 1981;114(2):555–62.

[11] Mountcastle WE, Compans RW, Lackland H, Choppin PW. Proteolytic cleavage of subunits of the nucleocapsid of the paramyxovirus simian virus 5. J Virol 1974;14(5):1253–61.

[12] Curran J, Homann H, Buchholz C, Rochat S, Neubert W, Kolakofsky D. The hypervariable C-terminal tail of the Sendai paramyxovirus nucleocapsid protein is required for template function but not for RNA encapsidation. J Virol 1993;67(7):4358–64.

[13] Nakamura J, Miyamoto T. Avianization of lapinized rinderpest virus. Am J Vet Res 1953;14(51):307–17.

[14] Morgan EM, Re GG, Kingsbury DW. Complete sequence of the Sendai virus NP gene from a cloned insert. Virology 1984;135(1):279–87.

Production of infectious hepatitis C virus particles in three-dimensional cultures of the cell line carrying the genome-length dicistronic viral RNA of genotype 1b

Kyoko Murakami [a], Koji Ishii [a], Yousuke Ishihara [b], Sayaka Yoshizaki [a], Keiko Tanaka [c], Yasufumi Gotoh [d,e], Hideki Aizaki [a], Michinori Kohara [f], Hiroshi Yoshioka [g], Yuichi Mori [g], Noboru Manabe [d], Ikuo Shoji [a], Tetsutaro Sata [c], Ralf Bartenschlager [h], Yoshiharu Matsuura [i], Tatsuo Miyamura [a], Tetsuro Suzuki [a,*]

[a] Department of Virology II, National Institute of Infectious Diseases, 1-23-1 Toyama, Shinjuku-ku, Tokyo 162-8640, Japan
[b] Hanaichi Ultrastructure Research Institute, Okazaki, Aichi 444-0076, Japan
[c] Department of Pathology, National Institute of Infectious Diseases, Shinjuku, Tokyo 162-8640, Japan
[d] Research Unit for Animal Life Sciences, Animal Resource Science Center, The University of Tokyo, Iwama, Ibaraki 319-0206, Japan
[e] Unit of Anatomy and Cell Biology, Department of Animal Sciences, Kyoto University, Kyoto 606-8502, Japan
[f] Department of Microbiology and Cell Biology, Tokyo Metropolitan Institute of Medical Science, Bunkyo-ku, Tokyo 113-8613, Japan
[g] Mebiol Inc., Hiratsuka, Kanagawa 254-0075, Japan
[h] Department of Molecular Virology, Hygiene Institute, University Heidelberg, Im Neuenhemier Feld 345, D-69120 Heidelberg, Germany
[i] Department of Molecular Virology, Research Institute for Microbial Diseases, Osaka University, Suita, Osaka 565-0871, Japan

Abstract

We show that a dicistronic hepatitis C virus (HCV) genome of genotype 1b supports the production and secretion of infectious HCV particles in two independent three-dimensional (3D) culture systems, the radial-flow bioreactor and the thermoreversible gelation polymer (TGP), but not in monolayer cultures. Immunoreactive enveloped particles, which are 50–60 nm in diameter and are surrounded by membrane-like structures, are observed in the culture medium as well as at the endoplasmic reticulum membranes and in dilated cytoplasmic cisternae in spheroids of Huh-7 cells. Infection of HCV particles is neutralized by anti-E2 antibody or patient sera that interfere with E2 binding to human cells. Finally, the utility of the 3D-TGP culture system for the evaluation of antiviral drugs is shown. We conclude that the replicon-based 3D culture system allows the production of infectious HCV particles. This system is a valuable tool in studies of HCV morphogenesis in a natural host cell environment.
© 2006 Elsevier Inc. All rights reserved.

Keywords: Hepatitis C virus; Replication; Three-dimensional culture; Virus particle

Introduction

Infection with hepatitis C virus (HCV) currently represents a major medical and socioeconomic problem. HCV is a main causative agent of chronic hepatitis, cirrhosis, and hepatocellular carcinoma, and there are an estimated 170 million HCV carriers worldwide (Choo et al., 1989). The standard treatments for HCV infection are interferon alpha (IFN-α) in combination with ribavirin (RBV) or, more recently, a polyethylene glycol-modified form of IFN-α; however, sustained response is seen in only ~50% of treated patients (Davis et al., 2003; Manns et al., 2001). Further development of new anti-HCV drugs and vaccines has been obstructed by the lack of either a small animal model or a robust cell culture system capable of supporting viral replication and the production of infectious progeny.

HCV is a small enveloped RNA virus belonging to the family Flaviviridae and harboring a single-stranded RNA genome with

positive polarity. A precursor polyprotein of ~3000 amino acids (aa) is encoded by a large open reading frame. This polyprotein is cleaved by cellular and viral proteases to give rise to a series of structural and nonstructural proteins (Choo et al., 1991; Grakoui et al., 1993; Hijikata et al., 1991). The establishment of selectable dicistronic HCV RNAs that are capable of autonomous replication in human hepatoma Huh-7 cells was a significant breakthrough in HCV research (Blight et al., 2000; Lohmann et al., 1999) and has provided an important tool for the study of HCV replication mechanisms and for screening antiviral drugs (Frese et al., 2001; Guo et al., 2001). This replicon system was first developed to replicate only viral subgenomic RNAs but has been further expanded to enable the replication of genome-length dicistronic RNAs (Ikeda et al., 2002; Pietschmann et al., 2002). Although the viral genome replicates and all HCV proteins are properly processed in this system, virus particle production has not yet been achieved. A number of researchers (Date et al., 2004; Kato et al., 2001, 2003) have developed an HCV genotype 2a replicon (JFH-1) that efficiently replicates in a variety of human cells. Recently, it has been demonstrated that the full-length JFH-1 genome or a chimeric genome using JFH-1 and J6, a related genotype 2a strain, produces infectious particles in cell cultures (Lindenbach et al., 2005; Wakita et al., 2005; Zhong et al., 2005). More recently, production of infectious genotype 1a virus (Hutchinson strain) using similar experimental systems has been described (Yi et al., 2006). These complete HCV culture systems produce robust levels of infectious virus and provides a powerful tool for HCV research. However, to date their applications have not been extended to constructs based on strains of genotype 1b, which is highly prevalent worldwide.

We previously demonstrated that differentiated human hepatoma FLC4 cells transfected with in vitro transcribed

HCV genomic RNA can produce and secrete infectious particles in three-dimensional (3D) radial-flow bioreactor (RFB) culture (Aizaki et al., 2003). This RFB system was initially aimed to develop artificial liver tissue, and the bioreactor column consists of a vertically extended cylindrical matrix through which liquid medium flows continuously from the periphery toward the center of the reactor (Kawada et al., 1998). In RFB culture, human hepatocellular carcinoma-derived cells can grow spherically or cubically, and they retain liver functions such as albumin synthesis (Kawada et al., 1998; Matsuura et al., 1998) and drug-metabolizing activity mediated by cytochrome P450 3A4 (Iwahori et al., 2003).

In the present study, two kinds of 3D culture techniques, the RFB and the thermoreversible gelation polymer (TGP), were used for the production and secretion of infectious HCV particles by using a dicistronic HCV genome derived from genotype 1b. We also demonstrate that these 3D culture systems are useful for evaluating anti-HCV drugs.

Results

Secretion of HCV-LPs from RCYM1 carrying genome-length dicistronic HCV RNA cultured in RFB culture

We first assessed the replicative capacity of selectable genome-length HCV RNAs in FLC4 cells. However, no G418-resistant colonies were observed, indicating that FLC4 cells do not support replication of these HCV RNAs (data not shown). Therefore, subsequent experiments were carried out with a stable Huh-7 cell line, RCYM1, which supports full-length HCV RNA replication and which was developed by transfection of the cells with genome-length dicistronic RNA derived from the Con1 clone I389neo/core-3'/NK 5.1 (genotype 1b)
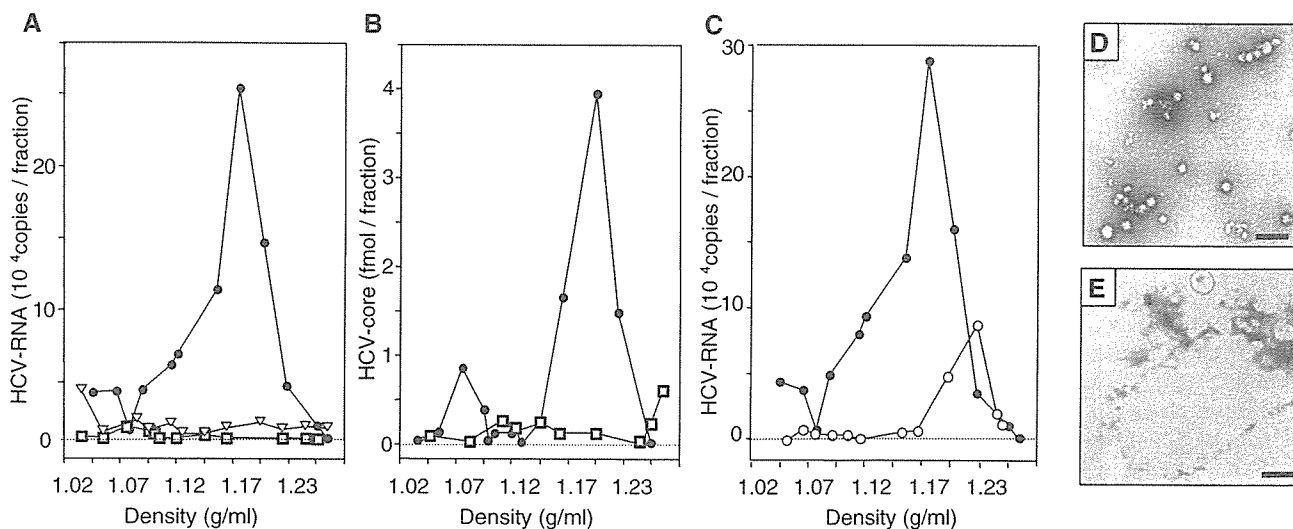

Fig. 1. Sucrose density gradient analysis of culture supernatants of RCYM1 cells. Culture media collected from radial-flow bioreactor (RFB)-cultured RCYM1 (closed circles), monolayer-cultured RCYM1 (open squares), and RFB-cultured 5–15 cells (open triangles) were fractionated as described in Materials and methods. (A) HCV RNA in each fraction was measured by real-time reverse transcriptase-polymerase chain reaction (RT-PCR). Mean values of duplicates were plotted against the density of the corresponding fraction. (B) HCV core protein in each fraction was determined by enzyme-linked immunosorbent assay (ELISA). Mean values of duplicates were plotted against the density. (C) Culture medium of RFB-cultured RCM1 cells were treated with 0.2% NP40 (open circles), followed by centrifugation in a sucrose gradient. Each fraction was tested for HCV RNA by real-time RT-PCR. (D, E) Electron microscopy analysis. Samples were prepared from the 1.18 g/ml fraction of culture media collected from RFB-cultured (D) or monolayer-cultured (E) RCYM1 cells.

(Pietschmann et al., 2002). The HCV RNA level in RCYM1 cells was approximately 5×10^6 copies/µg total RNA as determined by real-time reverse transcriptase-polymerase chain reaction (RT-PCR). The expression and subcellular localization of HCV protein were confirmed by Western blotting and immunofluorescence analysis (data not shown). To develop 3D RFB cultures, first we loaded RCYM1 cells onto an RFB column by flowing cell suspension, after which the cells were attached to carrier beads. Cells proliferated within the 3D matrix, and culture medium was circulated radially through the column.

In order to investigate whether HCV-like particles (HCV-LPs) were secreted from RCYM1 cells in the RFB culture system, we fractionated culture fluid collected after 5–10 days of culture by continuous 10–60% (wt/vol) sucrose density gradient centrifugation. HCV RNA and core protein were predominantly detected in the 1.15–1.20 g/ml fractions, with maximal detection in the 1.18 g/ml fraction (Figs. 1A and B). In the same experiment using 5–15 cells, in which a subgenomic HCV replicon replicates, no peak similar to that observed in RCYM1 cells corresponding to HCV RNA was detected. In both RCYM1 cells and 5–15 cells in the RFB culture system, a substantial amount of HCV RNA was detected in the 1.03–1.07 g/ml fractions (Fig. 1A). Consistent with a previous report by Pietschmann et al. (2002), these RNAs released from cells with a subgenomic replicon did not correspond to virus particles. When an equivalent number of RCYM1 cells were cultured in a monolayer culture system, limited amounts of HCV RNA and core protein were detected in the culture supernatant (Figs. 1A and B).

The mature HCV virion is thought to have a nucleocapsid and an outer envelope composed of a lipid membrane with viral envelope glycoproteins. Culture fluids were treated with NP40 in order to solubilize lipids and were then subjected to sucrose density gradient centrifugation. HCV RNA sedimented to a density of 1.22 g/ml rather than 1.18 g/ml (Fig. 1C), indicating that the density of HCV particles became higher due to de-envelopment. Transmission electron microscopy (TEM) of the 1.18 g/ml fraction, which was subjected to negative staining after concentration, revealed particle structures with diameters of 30–60 nm and a major particle size of 50 nm (Fig. 1D). No similar particle-like structures were observed in the same density fraction of the RCYM1 monolayer culture (Fig. 1E) or in the 1.23 g/ml fraction of the RCYM1-RFB culture (data not shown). These results indicate that, in the RFB system, the production and secretion of HCV-LPs is possible with a selectable dicistronic HCV genome.

Production and secretion of HCV-LPs from spheroid culture of RCYM1 cells using TGP

In the 3D RFB culture system for RCYM1 cells, extracellular secretion of HCV-LPs was observed. Based on this observation, we hypothesized that morphological changes occurring in 3D culture, such as polarity formation, promote advantageous in the assembly of viral proteins, particle formation, and extracellular secretion. To examine whether similar phenomena could be observed in other 3D culture systems, we investigated HCV-LP expression using a 3D culture system with TGP as a carrier.

TGP is a biocompatible polymer made from conjugates of polyethyleneglycol and poly-N-isopropylacrylamide, which is a thermoresponsive polymer composed of N-isopropylacrylamide and n-butylmethacrylate. The TGP solution possesses sol-gel transition properties; it is water soluble (sol phase) at temperatures below the transition temperature, and it is insoluble (gel phase) above it. It is possible to manipulate the transition temperatures through molecular engineering. The transition temperature for TGP in the present experiments was approximately 20 °C.
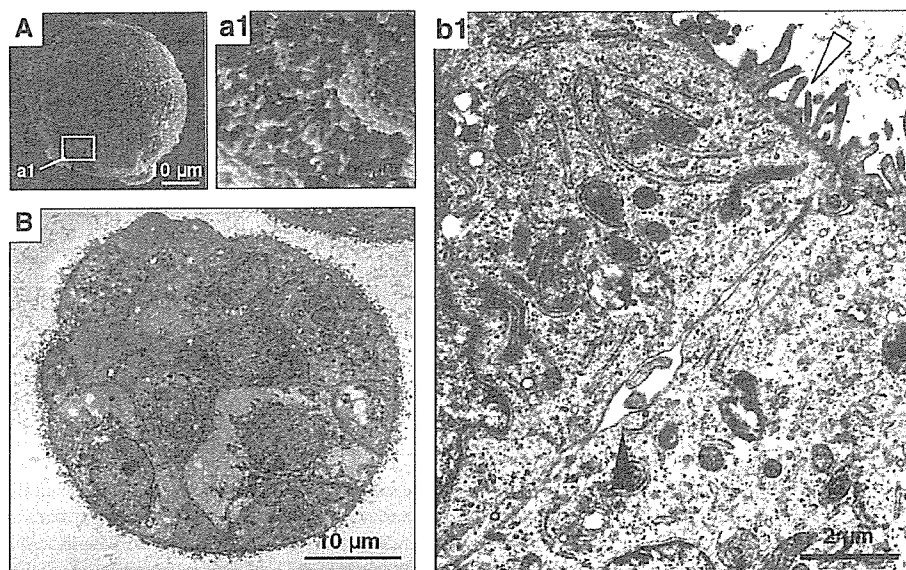

Fig. 2. Huh-7 and RCYM1 cells form spheroids in thermoreversible gelation polymer (TGP). Scanning electron microscopy (A and a1) and transmission electron microscopy (B and b1) of RCYM1 cells cultured in TGP for 8 days. Open arrowhead, microvilli; closed arrowheads, bile canaliculi-like structures.

RCYM1 cells, which were seeded into the TGP, formed three-dimensional compacted aggregates called spheroids after 3 days of culture, and numerous spheroids with diameters of approximately 1 mm were observed after 7–10 days of culture. After 8 days of culture, the spheroids were fixed and examined by scanning electron microscopy (Figs. 2A and a1) and ultrathin sections were examined by TEM (Figs. 2B and b1). Well-developed microvilli, a feature of polarized epithelium, were observed on the cell surface (Figs. 2A and a1). Bile canaliculi-like structures were also observed within intercellular spaces, and they appeared to be connected via tight junctions (Figs. 2B and b1). This cytomorphology, similar to that observed in the RFB culture (Kawada et al., 1998; Matsuura et al., 1998), correlated well with the features of mature liver tissue.

It is known that the replication of HCV replicons in Huh-7 cells depends on host cell growth. We found that the growth of RCYM1 cells in the TGP culture system was significantly slower than that of cells in monolayer culture (Fig. 3A). Accordingly, the expression of HCV proteins (Fig. 3B) in the

RCYM1 spheroids was apparently lower compared to those observed in the monolayer cells. The viral RNA copy number in the spheroids was approximately one tenth of that in the monolayer culture (data not shown). The results of sucrose density gradient analysis of culture supernatant demonstrated co-sedimentation of HCV RNAs and core proteins at a density of 1.15–1.20 g/ml, with a peak at 1.18 g/ml (Figs. 3C and D). This distribution was consistent with the pattern obtained in RFB culture (Figs. 1A and B). It should be noted that in these experiments, lower cell numbers were used in the 3D cultures than in the monolayer cultures because of the slower growth of cells. As estimated from the quantitative data of the 1.15–1.20 g/ml fractions of the culture supernatants, 0.1–1 copies of HCV RNA/cell/day are produced and assembled into viral particles in the TGP-cultured RCYM1 cells.

TEM analysis of the 1.18 g/ml fraction after negative staining showed particle structures with a diameter of 50–60 nm and spike-like projections (Fig. 3E). Observation of ultrathin sections indicated a lipid bilayer-like membrane structure with a
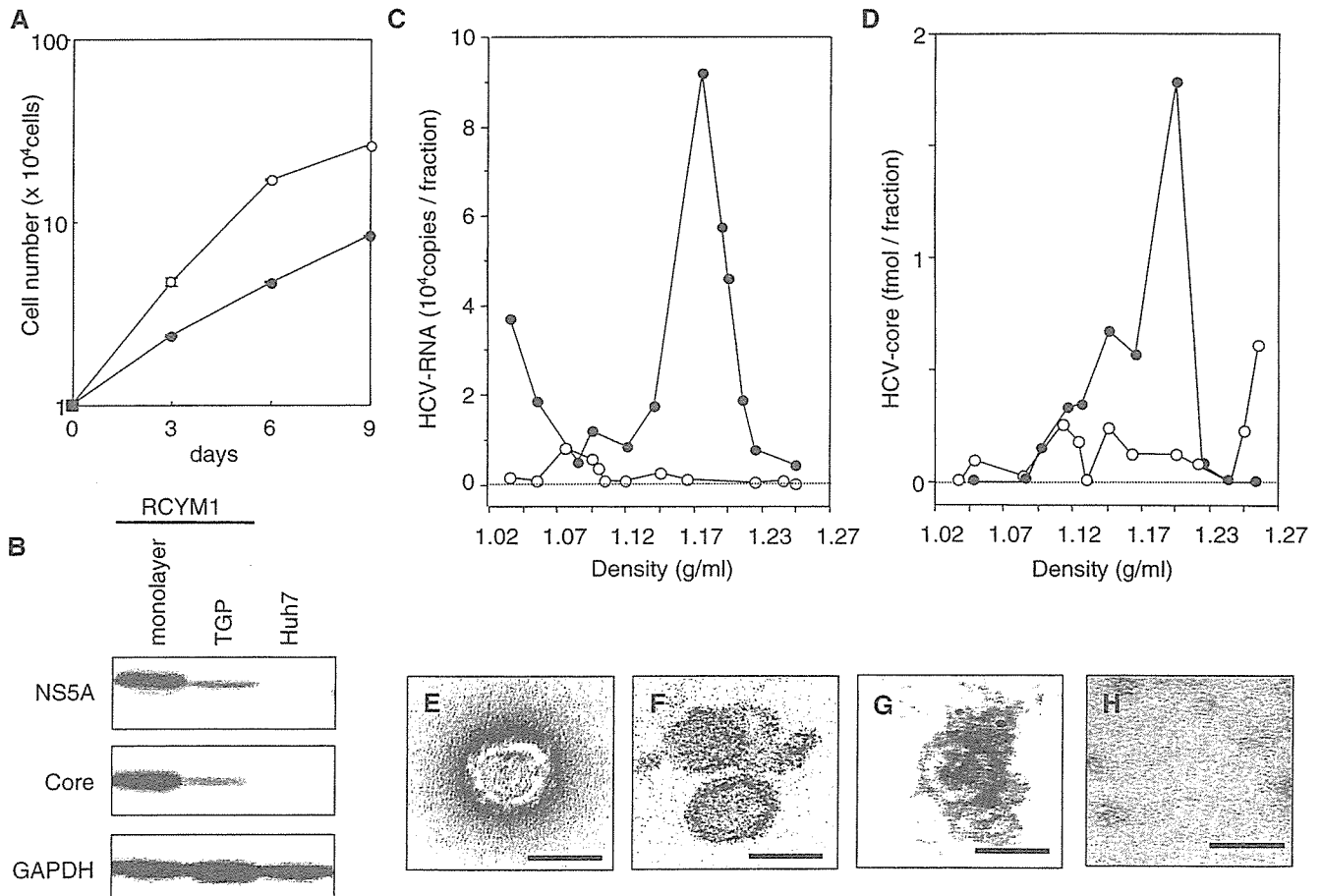

Fig. 3. Expression of HCV proteins in RCYM1 cells and secretion of viral particles in TGP culture. (A) Cell growth curves of the TGP (closed circles) and monolayer (open circles) culture of RCYM1 cells. Cells were harvested at days 0, 3, 6, and 9 postinoculation and cell numbers were determined. (B) Western blotting of HCV core and NS5A proteins in RCYM1 cells and control Huh-7 cells. (C, D) Sucrose density gradient analysis of culture supernatants of RCYM1 cells. The culture supernatants were fractionated as described in Materials and methods. HCV RNA (C) and core protein (D) in each fraction were determined by ELISA and real-time RT-PCR, respectively. Representative data from three independent experiments are shown. Closed circles, TGP culture; open circles, monolayer culture. (E–H) Electron microscopy of HCV-like particles (HCV-LPs) in the supernatants of TGP-cultured RCYM1 cells. (E) Negative staining of HCV-LPs in the 1.18 g/ml density fraction. There was no spherical structure in 1.05 g/ml density fraction, as shown in panel H. (F) Ultrathin section of HCV-LPs. Precipitated HCV-LP samples were prepared from the 1.18 g/ml fraction as described in Materials and methods. (G) Immunogold labeling of HCV-LPs with an anti-E2 antibody in the 1.18 g/ml density fraction. Gold particles, 5 nm; scale bars, 50 nm.
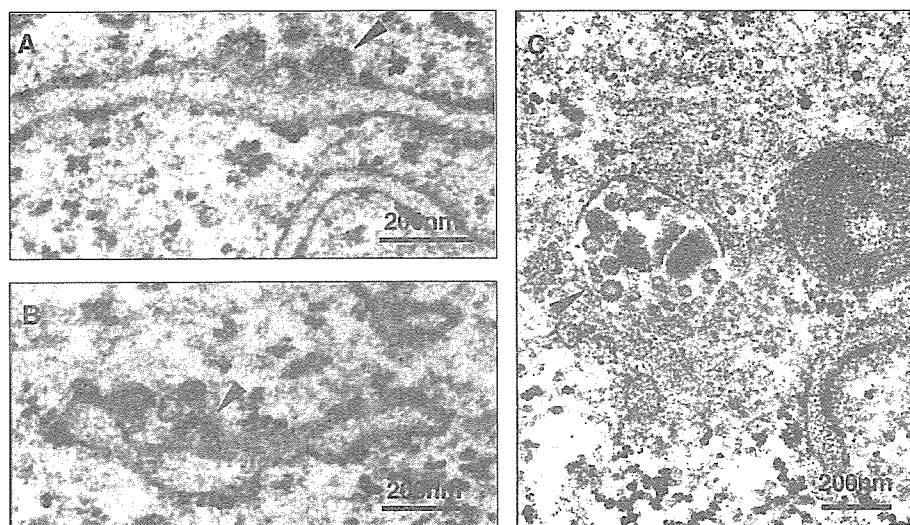
Fig. 4. Electron microscopy of ultrathin sections of RCYM1 cells grown in TGP. HCV-LPs in TGP-cultured RCYM1 cells. Spherical virus-like particles 50–60 nm in diameter (arrowheads) were observed at the ER membranes (A, B) and in the cytoplasmic vesicles (C).

width of approximately 5 nm (Fig. 3F). Immunoelectron microscopic study using anti-E2 antibody revealed HCV envelope protein(s) on the particle surface (Fig. 3G). Substantial amounts of HCV RNA were detected in the 1.03–1.05 g/ml fractions of the supernatant (Fig. 3C); however, HCV-LP structures were not observed in these fractions (Fig. 3H). These results were consistent with those from the RFB system, as shown above. The efficacy of 3D cell culture systems in virion formation was thus demonstrated in both the RFB and TGP culture systems using human liver-derived cells.

Ultrastructural localization of HCV-LPs in TGP-cultured spheroids of RCYM1 cells

We next determined the intracellular localization of HCV-LPs produced in RCYM1-TGP culture at the ultrastructural level by electron microscopic (EM) analysis of ultrathin sections. Spherical particles having membrane-like structures with short surface projections (diameter, 50–60 nm) were observed primarily at the endoplasmic reticulum (ER) membrane (Fig. 4A) as well as in the dilated cisternae of the ER (Fig. 4B). In vesicles, these virus-like particles were frequently associated with amorphous materials (Fig. 4C). In a previous study, Shimizu et al. (1996) report that virus-like particles with similar morphology and size were observed in human B cells infected with HCV. No similar particle-like structures were observed in RCYM1 cells in monolayer culture or in subgenomic replicon 5–15 in cells in TGP culture (data not shown).

In order to determine whether the virus-like particles observed by conventional TEM in the present experiment were HCV-LPs, we conducted immunoelectron microscopic analysis with anti-core antibody and anti-E1 antibody. Double-labeling experiments showed that the virus-like particles associated with the ER membrane exhibited immunoreactivity for both HCV proteins, and that the E1 protein surrounded the core proteins (Fig. 5A). To the best of our knowledge, this is the first report to clearly demonstrate that the viral envelope protein surrounds the core protein in HCV particle formation. As a negative control, thin sections prepared from subgenomic RNA containing 5–15 cells were stained with these antibodies and were found to exhibit negligible levels of background immunostaining (data not shown).
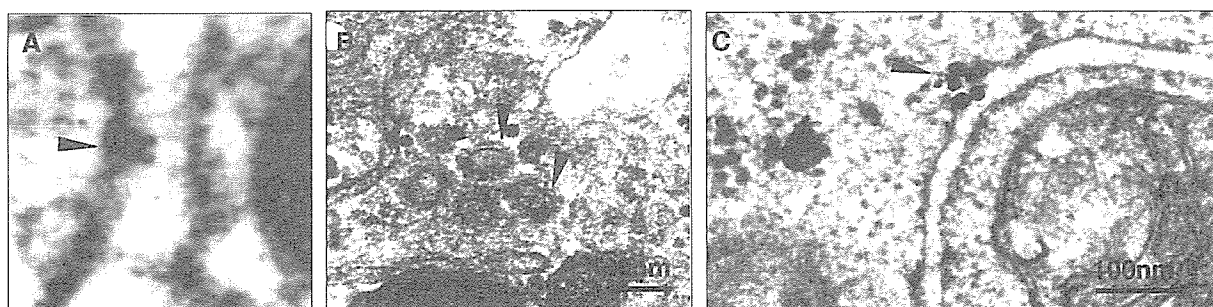

Fig. 5. Immunoelectron microscopy of ultrathin sections of TGP-cultured RCYM1 cells. (A) Double immunostaining with anti-E1 and anti-core monoclonal antibodies. Core protein-specific gold particles (10 nm in diameter) and E1 protein-specific gold particles (5 nm in diameter) formed rosettes on the surface of the ER membrane. (B and C) Silver-intensified immunogold staining with anti-core (B) and anti-E1 (C) antibodies. The second antibody conjugated with gold particles 1.4 nm in diameter was applied, followed by enlargement of the particles by the silver enhancement reagent. Arrowheads indicate virus-like particles reacting with anti-core and/or anti-E1 antibodies.